PHYSICAL REVIEW B **78**, 045118 (2008)

Calculation of the conductance of a graphene sheet using the Chalker-Coddington network model

I. Snyman,[1] J. Tworzydło,[2] and C. W. J. Beenakker[1]
[1]*Instituut-Lorentz, Universiteit Leiden, P.O. Box 9506, 2300 RA Leiden, The Netherlands*
[2]*Institute of Theoretical Physics, Warsaw University, Hoża 69, 00-681 Warsaw, Poland*
(Received 14 March 2008; revised manuscript received 9 June 2008; published 25 July 2008)

The Chalker-Coddington network model (introduced originally as a model for percolation in the quantum Hall effect) is known to map onto the two-dimensional Dirac equation. Here we show how the network model can be used to solve a scattering problem in a weakly doped graphene sheet connected to heavily doped electron reservoirs. We develop a numerical procedure to calculate the scattering matrix with the aide of the network model. For numerical purposes, the advantage of the network model over the honeycomb lattice is that it eliminates intervalley scattering from the outset. We avoid the need to include the heavily doped regions in the network model (which would be computationally expensive) by means of an analytical relation between the transfer matrix through the weakly doped region and the scattering matrix between the electron reservoirs. We test the network algorithm by calculating the conductance of an electrostatically defined quantum point contact and comparing with the tight-binding model of graphene. We further calculate the conductance of a graphene sheet in the presence of disorder in the regime where intervalley scattering is suppressed. We find an increase in conductance that is consistent with previous studies. Unlike the tight-binding model, the network model does not require smooth potentials in order to avoid intervalley scattering.

DOI: 10.1103/PhysRevB.78.045118 PACS number(s): 73.50.Td, 73.23.−b, 73.23.Ad, 73.63.−b

I. INTRODUCTION

The low-energy and long-wavelength properties of conduction electrons in a carbon monolayer (graphene) are described by the two-dimensional Dirac equation.[1] In one-dimensional geometries this partial differential equation can be solved analytically, but fully two-dimensional problems typically require a discretization to permit a numerical solution. The tight-binding model on the honeycomb lattice of carbon atoms provides the most obvious and physically motivated discretization.[2] The band structure of a honeycomb lattice has two valleys, coupled by potential variations on the scale of the lattice constant. Smooth potentials are needed if one seeks to avoid intervalley scattering and obtain the properties of a single valley.

Discrete representations of the Dirac equation that eliminate from the outset the coupling to a second valley may provide a more efficient way to isolate the single-valley properties. Alternative tight-binding models[3–6] have been introduced for that purpose. One method of discretization, which has received much attention, is the network model, originally introduced by Chalker and Coddington[7] as a model for percolation in the quantum Hall effect. Ho and Chalker[8] showed how a solution of this model can be mapped onto an eigenstate of the Dirac equation, and this mapping has proven to be an efficient way to study the localization of Dirac fermions.[9]

The recently developed capability to do transport measurements in graphene[10] has renewed the interest in the network model[11] and also raises some questions which have not been considered before. The specific issue that we address in this paper is how to introduce metallic contacts in the network model of graphene. Metallic contacts are introduced in the Dirac equation by means of a downward potential step of magnitude U_∞. The limit $U_\infty \to \infty$ is taken at the end of the calculation. (It is an essential difference with the Schrödinger equation that an infinite potential step produces a *finite* contact resistance in the Dirac equation.) This phenomenological model of metallic leads, introduced in Ref. 12, is now commonly used because (1) it is analytically tractable, (2) it introduces no free parameter, and (3) it agrees well with more microscopic models.[13,14] A direct implementation of such a metallic contact in the network model is problematic because the mapping onto the Dirac equation breaks down in the limit $U_\infty \to \infty$. Here we show how this difficulty can be circumvented.

To summarize then, there is a need to develop numerical methods for Dirac fermions in graphene when the potential landscape does not allow analytical solutions. If one implements a method based on the honeycomb lattice of graphene, intervalley scattering is present, unless the potential is smooth on the scale of the lattice. Smooth potential landscapes are experimentally relevant, but computationally expensive, because they require discretization with a large mesh. It is therefore preferable to develop a numerical method that eliminates intervalley scattering from the outset. The known correspondence between the Chalker-Coddington network model and the Dirac equation provides such a method, as we show in this paper. The key technical result of our work is an analytical method to include heavily doped reservoirs. (Including these reservoirs numerically would have been prohibitively expensive, computationally.)

In Secs. II and III we summarize the basic equations that we will need—first regarding the Dirac equation and then regarding the network model. Our key technical result in Sec. IV is a relationship between the scattering problems for the Dirac equation in the limit $U_\infty \to \infty$ and for the network model at $U_\infty \equiv 0$. We test the method in Sec. V by calculating the conductance of an electrostatically defined constriction (quantum point contact) in a graphene sheet. We also study

 ©2008 The American Physical Society

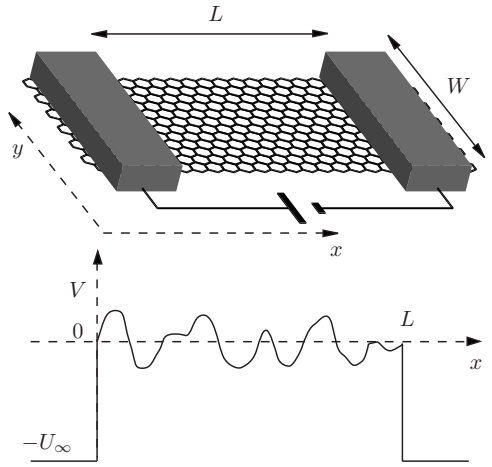

FIG. 1. Top panel: Schematic of a graphene sheet contacted by two electrodes. A voltage source drives a current through the sheet. The bottom panel shows the potential profile $V(x,y)$ for fixed y.

the effect of disorder on conductance. We confirm the results of previous studies[15–18] that smooth disorder (that does not cause intervalley scattering) enhances the conductivity of undoped graphene. We conclude in Sec. VI.

II. FORMULATION OF THE SCATTERING PROBLEM

A. Scattering matrix

A scattering formulation of electrical conduction through a graphene sheet was given in Ref. 12. We summarize the basic equations. The geometry, shown in Fig. 1, consists of a weakly doped graphene sheet (length L and width W) connected to heavily doped graphene leads. A single valley has the Dirac Hamiltonian

$$H = v\boldsymbol{\sigma}\cdot[\boldsymbol{p} - e\boldsymbol{A}(\boldsymbol{r})] + V(\boldsymbol{r}) + \sigma_z\mu(\boldsymbol{r}), \tag{2.1}$$

where $\boldsymbol{A}(\boldsymbol{r})$ is the magnetic vector potential, $V(\boldsymbol{r})$ is the electrostatic potential, and $\mu(\boldsymbol{r})$ is a substrate-induced mass term. The vector $\boldsymbol{\sigma}=(\sigma_x,\sigma_y)$ contains the standard Pauli matrices

$$\sigma_x = \begin{pmatrix} 0 & 1 \\ 1 & 0 \end{pmatrix}, \quad \sigma_y = \begin{pmatrix} 0 & -i \\ i & 0 \end{pmatrix}. \tag{2.2}$$

We assume that the fields $\boldsymbol{A}$, V, and μ are smooth on the scale of the lattice constant, so that the valleys are uncoupled.

In the heavily doped leads (for $x<0$ and $x>L$), we set $V(\boldsymbol{r})=-U_\infty$ and take the limit $U_\infty\to\infty$. For simplicity we set $\mu=0$ in the leads and we also assume that the magnetic field is zero in the leads (so $\boldsymbol{A}$ is constant there). The Dirac equation

$$H\Psi = E\Psi \tag{2.3}$$

has to be solved subject to boundary conditions on the wave function $\Psi(\boldsymbol{r})$ at $y=0$ and $y=W$. We will consider two types of boundary conditions, which mix neither valleys nor transverse modes. The first is the periodic boundary condition $\Psi|_{y=0}=\Psi|_{y=W}$. The second is the infinite-mass boundary condition[19]

$$\Psi|_{y=0} = \sigma_x\Psi|_{y=0}, \quad \Psi|_{y=W} = -\sigma_x\Psi|_{y=W}. \tag{2.4}$$

We consider a scattering state Ψ_n that has unit incident current from the left in mode n and zero incident current from the right. (The quantum number n labels transverse modes.) In the leads Ψ_n has the form

$$\Psi_n(\boldsymbol{r}) = \chi_n^+(y)e^{ik_nx} + \sum_m r_{mn}\chi_m^-(y)e^{-ik_mx}, \quad x<0, \tag{2.5a}$$

$$\Psi_n(\boldsymbol{r}) = \sum_m t_{mn}\chi_m^+(y)e^{ik_m(x-L)}, \quad x>L. \tag{2.5b}$$

We have introduced transmission and reflection amplitudes t_{mn} and r_{mn} and the longitudinal component k_n of the wave vector of mode n. The right-propagating component in mode n has a spinor χ_n^+ and the left-propagating component has a spinor χ_n^-.

In the limit $U_\infty\to\infty$, the form of the scattering state in the leads can be simplified considerably. The n dependence of k_n can be neglected, since $k_n\simeq U_\infty/\hbar v\to\infty$ as $U_\infty\to\infty$. The number $N_\infty\simeq U_\infty W/\hbar v$ of propagating modes in the leads can be taken infinitely large. When $N_\infty\to\infty$, the choice of boundary condition in the leads (not in the sample) becomes irrelevant and we choose periodic boundary conditions in the leads for simplicity. Modes that are responsible for transport through the weakly doped sample have transverse momenta $|q_n|\ll U_\infty$. The corresponding spinors $\chi_n^\pm$ are

$$\chi_n^\pm(y) = \frac{1}{\sqrt{2W}}e^{iq_ny}\begin{pmatrix} 1 \\ \pm 1 \end{pmatrix}, \quad q_n = \frac{2\pi n}{W}, \tag{2.6}$$

with $n=0,\pm1,\pm2,\ldots$. While it is important not to neglect the finiteness of q_n in the phase factor $\exp(iq_ny)$ of these modes, the spinor structure is proportional to $(1,\pm1)$, independent of n because $q_n/U_\infty\to0$. We note the orthogonality relation

$$\int_0^W dy\,\chi_m^\sigma(y)^\dagger\chi_n^{\sigma'}(y) = \delta_{m,n}\delta_{\sigma,\sigma'}. \tag{2.7}$$

We also note that the definition of $\chi_n^\pm(y)$ ensures that each scattering state Ψ_n carries unit incident current.

In a similar way, we can define a scattering state incident from the right in mode n with transmission and reflection amplitudes t'_{mn} and r'_{mn}. The transmission and reflection amplitudes constitute the scattering matrix

$$S = \begin{pmatrix} r & t' \\ t & r' \end{pmatrix}, \tag{2.8}$$

which is a unitary matrix that determines transport properties. For example, the conductance G follows from the Landauer formula

$$G = \frac{4e^2}{h}\mathrm{Tr}\,tt^\dagger = \frac{4e^2}{h}\mathrm{Tr}\,t't'^\dagger, \tag{2.9}$$

where the factor of 4 accounts for spin and valley degeneracies.

B. Transfer matrix

The information contained in the scattering matrix S can equivalently be represented by the transfer matrix T. While the scattering matrix relates outgoing waves to incoming waves, the transfer matrix relates waves at the right,

$$\Psi_R(\boldsymbol{r}) = \sum_{n,\sigma} b_n^\sigma \chi_n^\sigma(y) e^{i\sigma k_n(x-L)}, \quad x > L, \tag{2.10}$$

to waves at the left,

$$\Psi_L(\boldsymbol{r}) = \sum_{n,\sigma} a_n^\sigma \chi_n^\sigma(y) e^{i\sigma k_n x}, \quad x < 0. \tag{2.11}$$

The relation takes the form

$$b_m^\sigma = \sum_{n,\sigma'} T_{m,n}^{\sigma,\sigma'} a_n^{\sigma'}. \tag{2.12}$$

The four blocks $T^{\sigma,\sigma'}$ of the transfer matrix are related to the transmission and reflection matrices by

$$r = -(T^{--})^{-1} T^{-+}, \tag{2.13a}$$

$$t = T^{++} - T^{+-}(T^{--})^{-1} T^{-+}, \tag{2.13b}$$

$$t' = (T^{--})^{-1}, \tag{2.13c}$$

$$r' = T^{+-}(T^{--})^{-1}. \tag{2.13d}$$

Unitarity of S implies for T the current conservation relation

$$T^{-1} = \Sigma_z T^\dagger \Sigma_z, \tag{2.14}$$

where Σ_z is a matrix in the space of modes with entries $(\Sigma_z)_{m,n} = \delta_{m,n}\sigma_z$ that are themselves 2×2 matrices. In terms of the transfer matrix the Landauer formula [Eq. (2.9)] can be written as

$$G = \frac{4e^2}{h} \mathrm{Tr}[(T^{--\dagger} T^{--})^{-1}]. \tag{2.15}$$

C. Real-space formulation

In order to make contact with the network model, it is convenient to change from the basis of transverse modes (labeled by the quantum number n) to a real-space basis (labeled by the transverse coordinate y). The real space transfer matrix $X_{y,y'}$ is defined by

$$\Psi(L,y) = \int_0^W dy' X_{y,y'} \Psi(0,y'), \tag{2.16}$$

where $\Psi(x,y)$ is any solution of the Dirac equation [Eq. (2.3)] at a given energy E. The kernel $X_{y,y'}$ is a 2×2 matrix, acting on the spinor Ψ. Because the integral [Eq. (2.16)] extends only over the weakly doped region, X does not depend on the potential U_∞ in the leads.

In view of the orthogonality relation [Eq. (2.7)], the real-space transfer matrix X is related to the transfer matrix T defined in the basis of modes in the leads by a projection onto $\chi_m^\pm$,

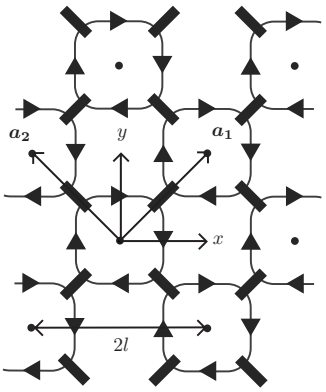

FIG. 2. Square lattice (dots), with circulating current loops that form the network model. The loops are coupled to nearest neighbors at the black rectangles. The lattice vectors $\boldsymbol{a}_1$ and $\boldsymbol{a}_2$ (each of length $\sqrt{2}l$) are indicated.

$$T_{m,n}^{\sigma,\sigma'} = \int_0^W dy \int_0^W dy' \chi_m^\sigma(y)^\dagger X_{y,y'} \chi_n^{\sigma'}(y'). \tag{2.17}$$

We now substitute the explicit form of χ_n^σ from Eq. (2.6). The integrals over y and y' in Eq. (2.17) amount to a Fourier transform,

$$X_{m,n} = \frac{1}{W} \int_0^W dy \int_0^W dy' e^{-iq_m y} X_{y,y'} e^{iq_n y'}. \tag{2.18}$$

From Eq. (2.17) we conclude that the 2×2 matrix structure of the transfer matrix,

$$T_{m,n} = \begin{pmatrix} T_{m,n}^{++} & T_{m,n}^{+-} \\ T_{m,n}^{-+} & T_{m,n}^{--} \end{pmatrix}, \tag{2.19}$$

is related to the 2×2 matrix structure of the real-space transfer matrix by a Hadamard transformation:

$$T_{m,n} = \mathcal{H} X_{m,n} \mathcal{H}, \quad \mathcal{H} = \frac{1}{\sqrt{2}} \begin{pmatrix} 1 & 1 \\ 1 & -1 \end{pmatrix}. \tag{2.20}$$

(The unitary and Hermitian matrix $\mathcal{H}$ is called the Hadamard matrix.) In view of Eq. (2.14), the current conservation relation for X reads

$$X^{-1} = \Sigma_x X^\dagger \Sigma_x, \quad (\Sigma_x)_{m,n} = \delta_{m,n}\sigma_x, \tag{2.21}$$

where we used $\mathcal{H}\sigma_z\mathcal{H} = \sigma_x$.

III. FORMULATION OF THE NETWORK MODEL

The Chalker-Coddington network model[7,9] was originally introduced in order to analyze the localization transition in the quantum Hall effect. Our interest in this model stems from the fact that it is known to map onto the two-dimensional Dirac equation.[8] We briefly recall how the network model is defined and how the mapping to the Dirac equation works. We consider the square lattice shown in Fig. 2, with lattice constant $\sqrt{2}l$ and lattice vectors

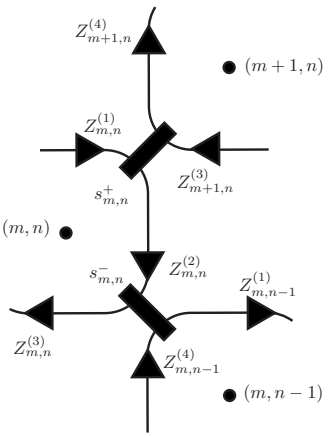

FIG. 3. Segment of the network of Fig. 2 with the wave amplitudes $Z^{(n)}_{m,n}$ and scattering matrices $s^{\pm}_{m,n}$ indicated.

$$\boldsymbol{a}_1 = l(\hat{\boldsymbol{x}} + \hat{\boldsymbol{y}}), \quad \boldsymbol{a}_2 = l(\hat{\boldsymbol{y}} - \hat{\boldsymbol{x}}). \tag{3.1}$$

The integers (m,n) label the lattice site $\boldsymbol{r}_{m,n} = m\boldsymbol{a}_1 + n\boldsymbol{a}_2$. With each site is associated a single current loop circling the site without enclosing any neighboring sites, say clockwise, if viewed from the positive z axis. The radii of these loops are expanded until states associated with nearest-neighboring sites overlap. At these points of overlap, states on adjacent loops can scatter into each other.

As illustrated in Fig. 3, four current amplitudes $Z^{(k)}_{m,n}$, $k = 1, \ldots, 4$ are associated with each site (m,n). These are amplitudes incident upon points of overlap, ordered clockwise, starting from the point of overlap with site $(m+1,n)$. Each incident wave amplitude $Z^{(k)}_{m,n}$ has picked up a phase $\phi^{(n)}_{m,n}$ since the previous point of overlap. With the point of overlap between loop (m,n) and $(m+1,n)$ is associated a 2×2 scattering matrix $s^{+}_{m,n}$, while $s^{-}_{m,n}$ is associated with the point of overlap between (m,n) and $(m,n-1)$.

The matrix elements of $s^{+}_{m,n}$ and $s^{-}_{m,n}$ are arranged such that

$$\begin{pmatrix} Z^{(2)}_{m,n} \\ Z^{(4)}_{m+1,n} \end{pmatrix} = \begin{pmatrix} e^{i\phi^{(2)}_{m,n}} & 0 \\ 0 & e^{i\phi^{(4)}_{m+1,n}} \end{pmatrix} s^{+}_{m,n} \begin{pmatrix} Z^{(1)}_{m,n} \\ Z^{(3)}_{m+1,n} \end{pmatrix}, \tag{3.2a}$$

$$\begin{pmatrix} Z^{(1)}_{m,n-1} \\ Z^{(3)}_{m,n} \end{pmatrix} = \begin{pmatrix} e^{i\phi^{(1)}_{m,n-1}} & 0 \\ 0 & e^{i\phi^{(3)}_{m,n}} \end{pmatrix} s^{-}_{m,n} \begin{pmatrix} Z^{(2)}_{m,n} \\ Z^{(4)}_{m,n-1} \end{pmatrix}. \tag{3.2b}$$

Ho and Chalker[8] showed how this model can be mapped onto the Dirac equation for two-dimensional fermions. Firstly, one parametrizes the scattering matrices $s^{\pm}_{m,n}$ in terms of Pauli matrices σ_i,

$$s^{-}_{m,n} = \sin\left(\frac{\pi}{4} + \beta_{m,n}\right)\sigma_z + \cos\left(\frac{\pi}{4} + \beta_{m,n}\right)\sigma_x, \tag{3.3a}$$

$$s^{+}_{m,n} = \cos\left(\frac{\pi}{4} + \beta_{m,n}\right)\sigma_z + \sin\left(\frac{\pi}{4} + \beta_{m,n}\right)\sigma_x. \tag{3.3b}$$

(The same matrix of coefficients $\beta_{m,n}$ is used for $s^{+}_{m,n}$ and $s^{-}_{m,n}$.) For given fields $V(\boldsymbol{r})$, $\boldsymbol{A}(\boldsymbol{r})$, and $\mu(\boldsymbol{r})$ in the Dirac equation, the mapping then dictates a corresponding choice of parameters in the network model, namely $\phi^{(k)}_{m,n}$ and $\beta_{m,n}$ have to satisfy[8]

$$\frac{1}{2}\sum_{k=1}^{4} \phi^{(k)}_{m,n} = [E - V(\boldsymbol{r}_{m,n})]\frac{l}{\hbar v}, \tag{3.4a}$$

$$\frac{\phi^{(1)}_{m,n} - \phi^{(3)}_{m,n}}{2} = A_x(\boldsymbol{r}_{m,n})\frac{el}{\hbar v}, \tag{3.4b}$$

$$\frac{\phi^{(4)}_{m,n} - \phi^{(2)}_{m,n}}{2} = A_y(\boldsymbol{r}_{m,n})\frac{el}{\hbar v}, \tag{3.4c}$$

$$2\beta_{m,n} = \mu(\boldsymbol{r}_{m,n})\frac{l}{\hbar v}. \tag{3.4d}$$

With this choice of parameters there is an approximate equality between a solution $\Psi(\boldsymbol{r})$ of the Dirac equation and the current amplitudes of the network model,

$$\Psi(\boldsymbol{r}_{m,n}) \approx \mathcal{G}\begin{pmatrix} Z^{(1)}_{m,n} \\ Z^{(3)}_{m,n} \end{pmatrix}, \quad \mathcal{G} = \frac{1}{\sqrt{2}}\begin{pmatrix} 1 & i \\ 1 & -i \end{pmatrix}. \tag{3.5}$$

The accuracy of the approximation is improved by making the lattice constant $\sqrt{2}l$ smaller and smaller.

As mentioned in Sec. II, we will be considering two types of boundary conditions at $y=0$ and $y=W$ in the sample region $0<x<L$. The periodic boundary condition is realized in the network model by putting the square lattice on a cylinder of circumference $W=2Nl$ oriented along the x axis. The infinite-mass boundary condition is realized[8] by terminating the square lattice at $y=0$ and $y=W$ and adjusting the scattering phases along the edge. The edge $y=0$ lies at sites $(n,-n)$ and the edge $y=W$ lies at sites $(N-1+n,N-1-n)$. As shown in Appendix A, for sites $(n,-n)$, Eq. (3.1) must be replaced with

$$Z^{(4)}_{n,-n} = -Z^{(3)}_{n,-n}, \quad Z^{(3)}_{n,-n} = Z^{(2)}_{n,-n}, \tag{3.6}$$

while for sites $(N+n,N-n)$ it must be replaced with

$$Z^{(2)}_{N+n,N-n} = Z^{(1)}_{N+n,N-n}, \quad Z^{(4)}_{N+n,N-n} = Z^{(1)}_{N+n,N-n}. \tag{3.7}$$

IV. CORRESPONDENCE BETWEEN SCATTERING MATRICES OF DIRAC EQUATION AND NETWORK MODEL

In this section we combine the known results summarized in the previous two sections to construct the scattering matrix S of a graphene strip with heavily doped leads from a solution of the network model. This construction does not immediately follow from the correspondence [Eq. (3.5)] because the limit $U_\infty \to \infty$ of heavily doped leads still needs to be taken. At first glance it would seem that in order to preserve the correspondence between the network model and the Dirac equation, we must simultaneously take the limit $l \to 0$ so that $U_\infty l/\hbar v$ remains small. (The correspondence between the network model and the Dirac equation is correct only to first-order in this quantity.) This would imply that very large

networks are required for an accurate representation of the graphene strip.

It turns out, however, that it is not necessary to model the heavily doped leads explicitly in the network model, as we now demonstrate. We define the real-space transfer matrix Y as the matrix that relates $Z^{(1)}$ and $Z^{(3)}$ at the right edge of the network to $Z^{(1)}$ and $Z^{(3)}$ at the left edge of the network. The left edge ($x=0$) lies at sites (n,n) with $n=0,1,2,\ \ldots,N-1$. The right edge at $x=L=2Ml$ lies at sites $(n+M,n-M)$. The real-space transfer matrix Y relates

$$\begin{pmatrix} Z^{(1)}_{n+M,n-M} \\ Z^{(3)}_{n+M,n-M} \end{pmatrix} = \sum_{n'=0}^{N-1} Y_{n,n'} \begin{pmatrix} Z^{(1)}_{n',n'} \\ Z^{(3)}_{n',n'} \end{pmatrix}. \tag{4.1}$$

We define the Fourier transform

$$Y_{q_m,q_n} = \frac{1}{N} \sum_{m'=0}^{N-1} \sum_{n'=0}^{N-1} e^{-2ilq_m m'} Y_{m',n'} e^{2ilq_n n'}, \tag{4.2}$$

with $q_n=2\pi n/W$.

In view of the relation [Eq. (3.5)] between the Dirac wave function Ψ and the network amplitudes $Z^{(1)}$, $Z^{(3)}$, the real-space transfer matrix X of the Dirac equation is related to Y by a unitary transformation,

$$X_{y=2ln,y'=2ln'} = \frac{1}{2l} \mathcal{G} Y_{n,n'} \mathcal{G}^{\dagger}. \tag{4.3}$$

We can now use the relation [Eq. (2.20)] between X and the transfer matrix T to obtain

$$T_{m,n} = \begin{pmatrix} 1 & 0 \\ 0 & i \end{pmatrix} Y_{q_m,q_n} \begin{pmatrix} 1 & 0 \\ 0 & -i \end{pmatrix}, \tag{4.4}$$

where we have used

$$\mathcal{H}\mathcal{G} = \begin{pmatrix} 1 & 0 \\ 0 & i \end{pmatrix}. \tag{4.5}$$

From Eq. (4.4) it follows that the lower right blocks of T and Y are equal: $T^{--}_{m,n}=Y^{--}_{q_m,q_n}$. Substitution into the Landauer formula (2.15) gives

$$G = \frac{4e^2}{h} \mathrm{Tr}[(Y^{--\dagger} Y^{--})^{-1}]. \tag{4.6}$$

The Landauer formula applied to the network model thus gives the conductance of the corresponding graphene sheet connected to heavily doped leads. For later use, we note the current conservation relation for Y, which follows from Eqs. (2.14) and (4.4)

$$Y^{-1} = \Sigma_z Y^{\dagger} \Sigma_z. \tag{4.7}$$

V. NUMERICAL SOLUTION

In this section we test the accuracy and efficiency of the solution of a scattering problem in graphene by means of the network model. As explained in Sec. VI we need to calculate the real-space transfer matrix Y through the weakly doped region. The conductance of the corresponding graphene sample then follows from Eq. (4.6).

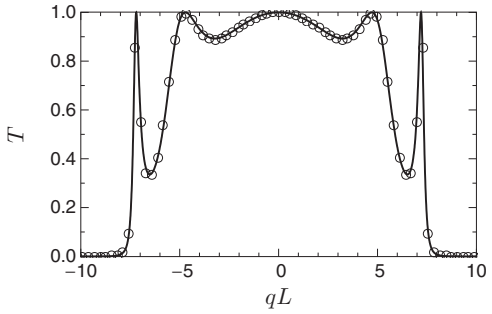

FIG. 4. Transmission probability of a clean graphene sheet at energy $E=7.85\hbar v/L$ as a function of transverse wave number q. The solid line is the result [Eq. (5.2)] from the Dirac equation, while the open circles were numerically calculated using the network model with periodic boundary conditions (when $q=2\pi n/W$). The discretization parameter of the network was $\epsilon=El/\hbar v=0.28$.

We calculate the real-space transfer matrix recursively by adding slices to the network and multiplying the transfer matrices of individual slices. Since a multiplication of transfer matrices is numerically unstable, we stabilize the algorithm as explained in Appendix B. We limit the numerical investigation in this section to the case $A(\boldsymbol{r})=0$, $\mu(\boldsymbol{r})=0$, where only the electrostatic potential $V(\boldsymbol{r})$ is nonzero.

We have found that the efficiency of the algorithm can be improved by using the fact that, according to Eq. (3.3), there is some arbitrariness in the choice of the phases $\phi^{(1)},\ \ldots,\phi^{(4)}$. For $\boldsymbol{A}(\boldsymbol{r})=0$ and $\mu(\boldsymbol{r})=0$, one choice of the phases could be

$$\phi^{(k)}_{m,n} = [E - V(m\boldsymbol{a}_1 + n\boldsymbol{a}_2)]l/2, \quad k=1,\ \ldots,4. \tag{5.1}$$

Another choice is

$$\phi^{(1)}_{m,n} = \phi^{(3)}_{m,n} = [E - V(\boldsymbol{r}_{m,n})]l, \quad \phi^{(2)} = \phi^{(4)} = 0. \tag{5.2}$$

The correspondence [Eq. (3.5)] between the network model and the Dirac equation holds for both choices of the phases; however the corrections for finite l are smaller for choice [Eq. (5.2)]. More precisely, as shown in Appendix C, if $\phi^{(2)}$ and $\phi^{(4)}$ are zero, the network model does not contain corrections to the Dirac equation of order $\boldsymbol{\partial}_r V l$.

Let us first consider the analytically solvable case of a clean graphene sheet that is obtained by setting $V=0$ in the weakly doped region. The Dirac equation gives transmission probabilities[12]

$$T(E,q) = \left| \cos \xi L + i \frac{E \sin \xi L}{\hbar v \xi} \right|^{-2}, \tag{5.3a}$$

$$\xi = \sqrt{\left(\frac{E}{\hbar v}\right)^2 - q^2}. \tag{5.3b}$$

For periodic boundary conditions the transverse wave vector is discretized as $q_n=2\pi n/W$, with $n=0,\pm 1,\pm 2,\ \ldots$

In Fig. 4 we compare Eq. (5.3) to the results from the network model for periodic boundary conditions in the weakly doped region. The small parameter that controls the

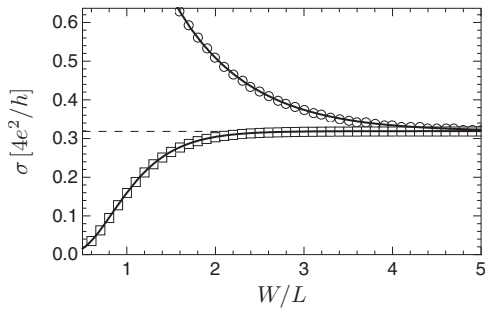

FIG. 5. Conductivity $\sigma=G\times L/W$ at $E=0$ for a clean graphene sheet as a function of the aspect ratio. The data points were calculated from the network model for fixed $L=40l$ with periodic boundary conditions (circles) and infinite-mass boundary conditions (squares) in the weakly doped region. The solid lines are the result (Ref. 12) from the Dirac equation. The dashed line indicates the limiting value $\sigma h/4e^2=1/\pi$ for short wide samples.

accuracy of the correspondence is $\epsilon=El/\hbar v$. We find excellent agreement for a relatively large $\epsilon\simeq 0.3$.

Figure 5 shows the conductivity

$$\sigma=\frac{L}{W}\frac{4e^2}{h}\sum_n T(E,q_n) \tag{5.4}$$

at the Dirac point ($E=0$) as a function of the aspect ratio W/L. We do the calculation both for periodic and infinite-mass boundary conditions in the weakly doped region. [In the latter case $q_n=(n+\frac{1}{2})\pi/W$ with $n=0,1,2,\ldots$.] Again we see excellent agreement with the analytical results from the Dirac equation.[12]

We now apply the network model to a case that cannot be solved analytically because it involves intermode scattering. We take the electrostatic potential landscape shown in Fig. 6, which produces a narrow constriction or quantum point contact of width D and length L_c. In the weakly doped region of length L, electrons have an energy E_F measured from the Dirac point. The barrier potential is tuned so that electron transport through the barrier takes place at the Dirac point, where all waves are evanescent. As the constriction is widened, the number of modes at a given energy that propagates through the opening increases. For fixed E_F, this should lead to steps in the conductance as a function of opening width, at intervals of roughly π/E_F. The steps are smooth because the current can also tunnel through the barrier.

We have calculated the conductance with the network model (solid curve in Fig. 7) and using the tight-binding

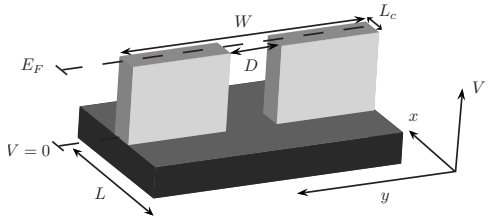

FIG. 6. Potential landscape $V(x,y)$ that produces a quantum point contact. The Fermi energy E_F is indicated.

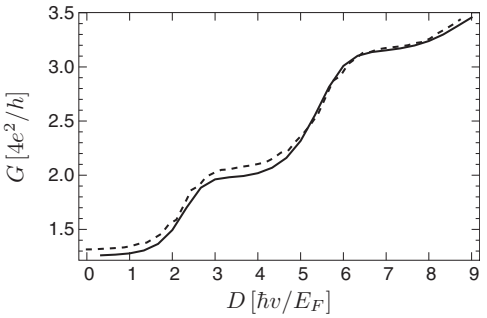

FIG. 7. Conductance through the constriction of Fig. 6 as a function of the width of the opening in the constriction. The solid line was obtained using the network model, while the dashed line was obtained using the tight-binding model of graphene. We used parameters $W=35\hbar v/E_F$, $L_c=8.7\hbar v/E_F$. For the network model we set the length of the weakly doped region to $L=49\hbar v/E_F$ and used a lattice constant $\sqrt{2}l=0.24\hbar v/E_F$, while in the tight-binding calculation we used a lattice constant $0.17\hbar v/E_F$.

model of graphene (dashed curve). In the tight-binding calculation we did not connect heavily doped leads to the weakly doped region. This does not affect the results, as long as $L\gg L_c$.

Both calculations show a smooth sequence of steps in the conductance. The agreement is reasonably good, but not as good as in the previous cases. This can be understood since the tight-binding model of graphene is only equivalent to the Dirac equation on long length scales.

The final numerical study that we report on in this paper involves transport at the Dirac point through a disordered potential landscape. Recent experimental studies[20] have observed electron and hole puddles in undoped graphene. The correlation length of the potential is larger than the lattice constant, hence intervalley scattering is weak. We are therefore in the regime of applicability of the network model (which eliminates intervalley scattering from the outset).

To model the electron and hole puddles, we divide the sample into an array of square tiles (Fig. 8), where each tile has size $10l\times 10l$, $\sqrt{2}l$ being the lattice constant of the network model. The electrostatic potential is constant on a

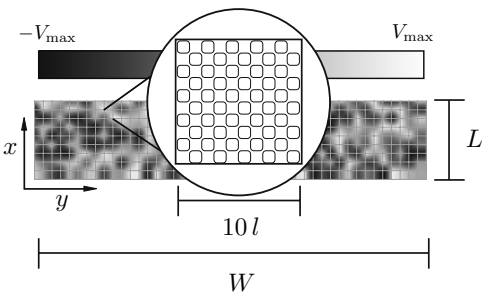

FIG. 8. Illustration of the model of electron and hole puddles in a graphene strip that we have studied. The sample is divided into tiles. The value of the potential on a tile is a constant, here indicated in grayscale, uniformly distributed between $-V_{\max}$ and $V_{\max}$. The potential on different tiles is uncorrelated. We choose a mesh for the network such that each tile has size $10l\times 10l$, where the network lattice constant is $\sqrt{2}l$.

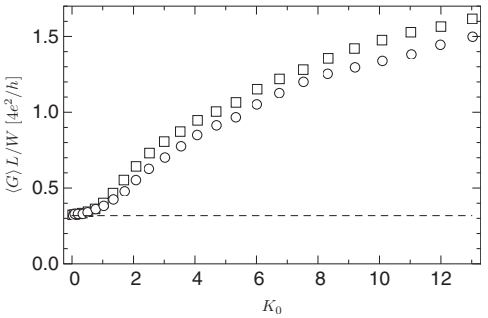

FIG. 9. Conductivity $\sigma = GL/W$ averaged over 100 disorder realizations versus disorder strength K_0 at the Dirac point $E=0$. The circles are for samples of size $60l \times 300l$ while squares are for samples of size $90l \times 450l$. The statistical error is of the order of the size of the data points. The dotted line indicates the ballistic limit $GL/W = 4e^2/\pi h$.

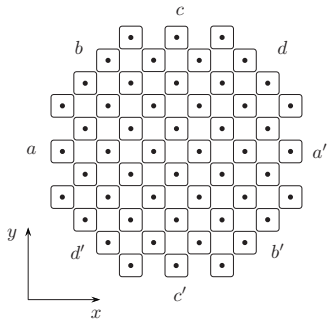

FIG. 10. Network of circulating current loops, as in Fig. 2, but now terminated with straight edges. The letters a, b, … label the orientation of the edge.

single tile, but uncorrelated with the potential on the other tiles. We take the values of the potential on any given tile to be a random variable uniformly distributed between $-V_{\max}$ and $V_{\max}$. To make contact with previous studies,[15,16] we quantify the disorder strength by the dimensionless number

$$K_0 = \frac{1}{(\hbar v)^2}\int d\boldsymbol{r}'\langle V(\boldsymbol{r})V(\boldsymbol{r}')\rangle. \tag{5.5}$$

[The average $\langle V(\boldsymbol{r})\rangle$ is zero.] With tiles of dimension $10l \times 10l$, the relation between K_0 and $V_{\max}$ is $K_0 = 100(V_{\max}l/\hbar v)^2/3$, and the network model faithfully represents the Dirac equation for values up to $K_0 \simeq 10$. We use a sample with aspect ratio $W/L=5$ and average over 100 disorder realizations. We repeat the calculation for two different sample sizes, namely $W=5L=300l$ and $W=5L=450l$. The calculation is performed for transport at energy $E=0$, i.e., the Dirac point of a clean, undoped sample. In Fig. 9 we show the average conductance. Remarkably enough, the conductance increases with increasing disorder strength. This is consistent with the results obtained in Refs. 15–18. The effect should not depend on the shape of the tiles in our model for the disorder. We have therefore repeated the calculation with rhombic instead of square tiles. We find deviations of less than 5%.

The increase in conductance is explained by the nonzero density of states at the Dirac point that is induced by the disorder, together with the absence of back-scattering for Dirac electrons. While we do not make a detailed study of the dependence of conductance on sample size (at fixed aspect ratio), we note that the conductance of larger samples (squares in Fig. 9) is larger than the conductance of the smaller samples (circles in Fig. 9). This is consistent with the scaling behavior found in Refs. 16–18.

VI. CONCLUSION

In conclusion, we have shown how the Chalker-Coddington network model can be used to solve a scattering problem in a weakly doped graphene sheet between heavily doped electron reservoirs (which model the metallic contacts). The method is particularly useful when the scattering problem does not allow an analytical solution, so that a numerical solution is required. The network model eliminates intervalley scattering from the outset. Thus, with a given mesh size, a larger graphene sample can be modeled with the network model than with methods based on the honeycomb lattice. The key technical result of our work is that an infinitely high potential step at the contacts can be implemented analytically by a unitary transformation of the real-space transfer matrix, without having to adjust the lattice constant of the network model to the small values needed to accommodate the small wavelength in the contacts. We have demonstrated that the algorithm provides an accuracy and efficiency comparable to the tight-binding model on a honeycomb lattice. In agreement with the existing literature[15–18] we have found that disorder that is smooth on the scale of the graphene lattice constant enhances conductivity at the Dirac point. The absence of intervalley scattering in the network model may prove useful for the study of these and other single-valley properties.

ACKNOWLEDGMENTS

This research was supported by the Dutch Science Foundation NWO/FOM and by the European Union's Marie Curie Research Training Network (contract MRTN-CT-2003–504574, Fundamentals of Nano-electronics).

APPENDIX A: INFINITE-MASS BOUNDARY CONDITION FOR THE NETWORK MODEL

In this appendix we consider the boundary condition imposed on the Dirac equation by termination of the network along a straight edge. We consider the eight orientations shown in Fig. 10, which have the shortest periodicity along the edge. Since we want to discuss the long-wavelength limit, each edge needs to be much longer than the lattice constant $\sqrt{2}l$. (In this respect the figure with its relatively short edges is only schematic.) The orientations are defined by the vector $\hat{\boldsymbol{n}}(\alpha) = -\hat{\boldsymbol{x}}\sin\alpha + \hat{\boldsymbol{y}}\cos\alpha$, $\alpha = j\pi/4$, $j = 1, \ldots, 8$, which is perpendicular to the edge and points outwards.

We wish to impose the infinite-mass boundary condition[21]

$$\Psi_{\text{edge}} = [\hat{\boldsymbol{n}}(\alpha) \times \hat{z}] \cdot \boldsymbol{\sigma} \Psi_{\text{edge}} = (\sigma_x \cos\alpha + \sigma_y \sin\alpha)\Psi_{\text{edge}} \tag{A1}$$

on the Dirac wave function at the edge. In view of the correspondence [Eq. (3.5)] between the Dirac equation and the network model, Eq. (A1) implies the boundary condition

$$\begin{pmatrix} Z^{(1)} \\ Z^{(3)} \end{pmatrix}_{\text{edge}} = (-\sigma_x \sin\alpha + \sigma_z \cos\alpha) \begin{pmatrix} Z^{(1)} \\ Z^{(3)} \end{pmatrix}_{\text{edge}} \tag{A2}$$

on the network amplitudes.

Away from the edge, the network amplitudes obey Eq. (3.1). For μ, $\boldsymbol{A}$, V, and E all equal to zero (Dirac point), these reduce to

$$\begin{pmatrix} Z^{(2)}_{m,n} \\ Z^{(4)}_{m+1,n} \end{pmatrix} = \mathcal{H} \begin{pmatrix} Z^{(1)}_{m,n} \\ Z^{(3)}_{m+1,n} \end{pmatrix}, \tag{A3a}$$

$$\begin{pmatrix} Z^{(1)}_{m,n-1} \\ Z^{(3)}_{m,n} \end{pmatrix} = \mathcal{H} \begin{pmatrix} Z^{(2)}_{m,n} \\ Z^{(4)}_{m,n-1} \end{pmatrix}. \tag{A3b}$$

We can eliminate the amplitudes $Z^{(2)}$ and $Z^{(4)}$ to arrive at the equations

$$Z^{(1)}_{m,n} = \frac{1}{2}[Z^{(1)}_{m,n+1} + Z^{(1)}_{m-1,n} - Z^{(3)}_{m,n} + Z^{(3)}_{m+1,n+1}], \tag{A4a}$$

$$Z^{(3)}_{m,n} = \frac{1}{2}[Z^{(1)}_{m,n} - Z^{(1)}_{m-1,n-1} + Z^{(3)}_{m+1,n} + Z^{(3)}_{m,n-1}]. \tag{A4b}$$

There are two linearly independent solutions $(Z^{(1)}_{m,n}, Z^{(3)}_{m,n}) \propto (1,0)$ and $(Z^{(1)}_{m,n}, Z^{(3)}_{m,n}) \propto (0,1)$. When the network is truncated along an edge, bulk Eqs. (A3a) and (A3b) do not hold for the amplitudes along the edge. We seek the modified equations that impose the boundary condition [Eq. (A2)] up to corrections of order $(E-V)l/\hbar v$.

The edge orientation a was previously considered by Ho and Chalker.[8] We consider here all four independent orientations a, b, c, and d. The other four orientations a', b', c', and d' are obtained by a symmetry relation.

Edge a is constructed by removing all sites (m,n) with $n > m$. (See Fig. 11.) This means that the network amplitudes $Z^{(3)}_{m,m}$ are prevented from scattering into the nonexistent amplitudes $Z^{(2)}_{m-1,m}$ belonging to the removed sites $(m-1,m)$. Similarly, the amplitudes $Z^{(4)}_{m,m}$ are prevented from scattering into the nonexistent amplitudes $Z^{(3)}_{m,m+1}$. To do this one must modify the scattering matrices $s^{+}_{m-1,m}$ so that $Z^{(3)}_{m,m}$ can only scatter into $Z^{(4)}_{m,m}$, and $s^{-}_{m,m+1}$ so that $Z^{(4)}_{m,m}$ can only scatter into $Z^{(1)}_{m,m}$. As a consequence, for $n = m+1$, Eq. (A2) is replaced by

$$Z^{(4)}_{m,m} = -Z^{(3)}_{m,m}, \quad Z^{(1)}_{m,m} = Z^{(4)}_{m,m}. \tag{A5}$$

We eliminate $Z^{(2)}$ and $Z^{(4)}$ to arrive at Eq. (A3) for $n < m$ and Eq. (A4) for $n = m$. Equation (A4) for $n = m$ is replaced by

$$Z^{(1)}_{m,m} = -Z^{(3)}_{m,m}. \tag{A6}$$

The solution $(Z^{(1)}_{m,n}, Z^{(3)}_{m,n}) \propto (1,-1)$ indeed satisfies the infinite-mass boundary condition [Eq. (A2)] with $\alpha = \pi/2$.

Edge b is constructed by removing all sites (m,n) with $n > 0$. (See Fig. 12.) This means that the network amplitudes

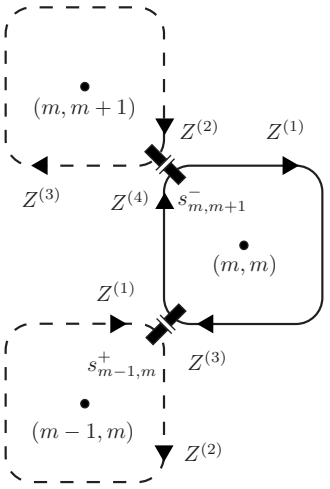

FIG. 11. Network amplitudes at an edge with orientation a. The dashed current loops are removed.

$Z^{(4)}_{m,0}$ are prevented from scattering into the nonexistent amplitudes $Z^{(3)}_{m,1}$ belonging to the removed sites $(m,1)$. For $n = 1$, we replace Eq. (A3) by

$$Z^{(1)}_{m,0} = Z^{(4)}_{m,0}. \tag{A7}$$

If we now eliminate the amplitudes $Z^{(2)}$ and $Z^{(4)}$, we find that Eq. (A3) is still valid for all $n < 0$. For $n = 0$, Eq. (A4) still holds, while Eq. (A4) is changed to

$$Z^{(1)}_{m,0} = \frac{1}{\sqrt{2}}[Z^{(1)}_{m-1,0} - Z^{(3)}_{m,0}]. \tag{A8}$$

The solution $(Z^{(1)}_{m,n}, Z^{(3)}_{m,n})^{\mathrm{T}} \propto (1, 1-\sqrt{2})$ satisfies the infinite-mass boundary condition [Eq. (A2)] with $\alpha = \pi/4$.

Next, we consider edge c, which results from the removal of all sites (m,n) with $m > -n$. (See Fig. 13.) In this case, $s^{-}_{m,-m+1}$ must be modified to prevent $Z^{(4)}_{m,-m}$ from scattering into $Z^{(3)}_{m,-m+1}$. Furthermore, $s^{+}_{m,-m}$ must be modified to prevent $Z^{(1)}_{m,-m}$ from scattering into $Z^{(4)}_{m+1,-m}$. For $n = -m+1$ we replace Eq. (A2) by

$$Z^{(2)}_{m,-m} = Z^{(1)}_{m,-m}, \quad Z^{(1)}_{m,-m} = Z^{(4)}_{m,-m}, \tag{A9}$$

and eliminate $Z^{(2)}$ and $Z^{(4)}$ to verify that the boundary condition holds.

The condition [Eq. (A9)] modifies three components of Eqs. (A3a) and (A3b):

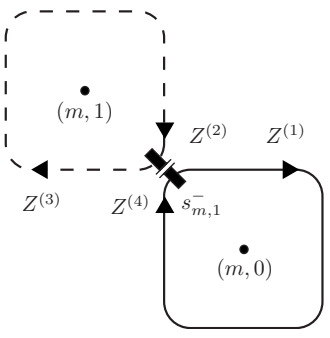

FIG. 12. Edge with orientation b.

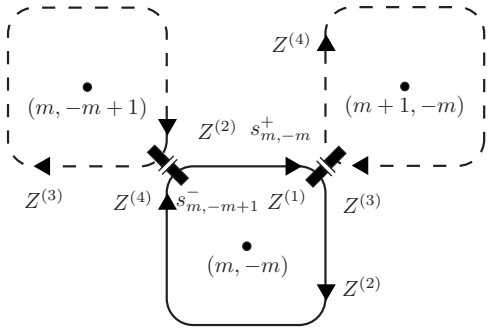

FIG. 13. Edge with orientation c.

$$Z^{(1)}_{m,-m} = \frac{1}{\sqrt{2}}[Z^{(1)}_{m-1,-m} - Z^{(3)}_{m,-m}], \tag{A10a}$$

$$Z^{(3)}_{m,-m} = \frac{1}{2}[Z^{(3)}_{m,-m-1} - Z^{(1)}_{m-1,-m-1} + \sqrt{2}Z^{(1)}_{m,-m}], \tag{A10b}$$

$$Z^{(1)}_{m,-m-1} = \frac{1}{2}[-Z^{(3)}_{m,-m-1} + Z^{(1)}_{m-1,-m-1} + \sqrt{2}Z^{(1)}_{m,-m}]. \tag{A10c}$$

For $m<-n-1$ Eq. (A3) holds without modification and Eq. (A3) also holds for $m=-n-1$. The solution

$$Z^{(1)}_{m,n<-m} = \sqrt{2}Z^{(1)}_{m,-m} = \text{constant}, \quad Z^{(3)}_{m,n} = 0 \tag{A11}$$

implies $(Z^{(1)}_{m,n}, Z^{(3)}_{m,n}) \propto (1,0)$ for $m<-n$, which satisfies the infinite-mass boundary condition [Eq. (A2)] with $\alpha=0$.

Edge d results from the removal of all sites (n,m) with $m>0$. (See Fig. 14.) We must modify $s^+_{0,m}$ such that $Z^{(1)}_{0,m}$ does not scatter into $Z^{(4)}_{1,m}$. To do this we replace Eq.(A3) for sites $(0,m)$ by

$$Z^{(2)}_{0,m} = Z^{(1)}_{0,m}. \tag{A12}$$

We again eliminate $Z^{(2)}$ and $Z^{(4)}$ to arrive at

$$Z^{(1)}_{0,m} = \frac{1}{\sqrt{2}}[\sqrt{2}Z^{(1)}_{0,m+1} + Z^{(1)}_{-1,m} - Z^{(3)}_{0,m}], \tag{A13a}$$

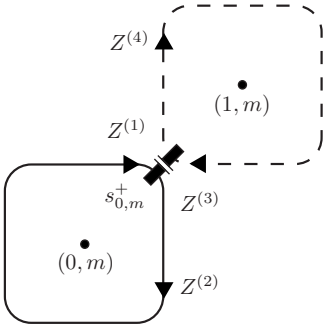

FIG. 14. Edge with orientation d.

$$Z^{(3)}_{0,m} = \frac{1}{\sqrt{2}}[\sqrt{2}Z^{(1)}_{0,m} - Z^{(1)}_{-1,m-1} + Z^{(3)}_{0,m-1}], \tag{A13b}$$

while for $m<0$ Eq. (A3) still holds. The solution $(Z^{(1)}_{m,n}, Z^{(3)}_{m,n}) \propto (1, \sqrt{2}-1)$ obeys the infinite-mass boundary condition [Eq. (A2)] with $\alpha=-\pi/4$, as required.

This completes the boundary conditions for the four orientations a, b, c, and d. The orientations a', b', c', and d' are obtained by the following symmetry: The network model is left invariant by a π rotation in coordinate space (which takes $\boldsymbol{r}$ to $-\boldsymbol{r}$) together with the application of σ_y in spinor space [which takes $Z^{(1)}$ to $-iZ^{(3)}$ and $Z^{(3)}$ to $iZ^{(1)}$].

APPENDIX B: STABLE METHOD OF MULTIPLICATION OF TRANSFER MATRICES

To construct the transfer matrix of a conductor, one can divide it into slices, compute the transfer matrix of each slice, and multiply the individual transfer matrices. This recursive construction is numerically unstable because products of transfer matrices contain exponentially growing eigenvalues, which overwhelm the small eigenvalues relevant for transport properties. Chalker and Coddington[7] used an orthogonalization method[22,23] to calculate the small eigenvalues in a numerically stable way. To obtain both eigenvalues and eigenfunctions, we employ an alternative method.[16,24] Using the condition of current conservation, the product of transfer matrices can be converted into a composition of unitary matrices, involving only eigenvalues of unit absolute value.

We briefly outline how the method works for the real-space transfer matrices Y of the network model, defined by Eq. (4.1). For the recursive construction it is convenient to rewrite this definition as

$$\begin{pmatrix} Z^{(1)}_{m+L,m-L} \\ Z^{(3)}_{m+L,m-L} \end{pmatrix} = \sum_{n=0}^{N-1} Y(L,L')_{m,n} \begin{pmatrix} Z^{(1)}_{n+L',n-L'} \\ Z^{(3)}_{n+L',n-L'} \end{pmatrix}. \tag{B1}$$

The numbers L,L' are integers so that $Y(L,L')$ is the transfer matrix from $x'=2L'l$ to $x=2Ll$. The composition law for transfer matrices is matrix multiplication,

$$Y(L,0) = Y(L,L-1)Y(L-1,0), \tag{B2}$$

with initial condition $Y(0,0)$= identity matrix.

The unstable matrix multiplication may be stabilized with the help of the condition $Y^{-1}=\Sigma_z Y^\dagger \Sigma_z$ of current conservation (see Sec. VI). Because of this condition, the matrix U constructed from Y by

$$Y = \begin{pmatrix} a & b \\ c & d \end{pmatrix} \Leftrightarrow U = \begin{pmatrix} -d^{-1}c & d^{-1} \\ a - bd^{-1}c & bd^{-1} \end{pmatrix} \tag{B3}$$

is a unitary matrix $(U^{-1}=U^\dagger)$. Matrix multiplication of Y's induces a nonlinear composition of U's,

$$Y_1 Y_2 \Leftrightarrow U_1 \otimes U_2, \tag{B4}$$

defined by

$$\begin{pmatrix} a_1 & b_1 \\ c_1 & d_1 \end{pmatrix} \otimes \begin{pmatrix} a_2 & b_2 \\ c_2 & d_2 \end{pmatrix} = \begin{pmatrix} a_3 & b_3 \\ c_3 & d_3 \end{pmatrix}, \tag{B5}$$

$$a_3 = a_1 + b_1(1 - a_2 d_1)^{-1} a_2 c_1, \tag{B6a}$$

$$b_3 = b_1(1 - a_2 d_1)^{-1} b_2, \tag{B6b}$$

$$c_3 = c_2(1 - d_1 a_2)^{-1} c_1, \tag{B6c}$$

$$d_3 = d_2 + c_2(1 - d_1 a_2)^{-1} d_1 b_2. \tag{B6d}$$

The algorithm now works as follows: Multiply a number of transfer matrices and stop well before numerical overflow would occur. Transform this transfer matrix into a unitary matrix according to Eq. (B3). Continue with the next sequence of transfer matrices, convert to a unitary matrix and convolute with the previous unitary matrix. At the end, we may transform back from U to Y by the inverse of relation (B3)

$$U = \begin{pmatrix} A & B \\ C & D \end{pmatrix} \Leftrightarrow Y = \begin{pmatrix} C - DB^{-1}A & DB^{-1} \\ -B^{-1}A & B^{-1} \end{pmatrix}. \tag{B7}$$

In practice this final transformation is unnecessary. According to Eq. (B3) the upper-right block of U is $d^{-1} \equiv (Y^{--})^{-1}$, which is all we need to calculate the conductance using the Landauer formula (4.6).

APPENDIX C: OPTIMAL CHOICE OF PHASES IN THE NETWORK MODEL

In Sec. V we noted that the same long-wavelength correspondence between the Dirac equation and the network model can be obtained for different choices of the phases $\phi^{(k)}_{m,n}$. Among these choices, choice (5.2) avoids corrections of order $\boldsymbol{\partial}_r V l$ to the Dirac equation. Here we show why.

For $\mu = \boldsymbol{A} = 0$ Eq. (3.3) reduces to

$$\beta_{m,n} = 0, \tag{C1a}$$

$$\phi^{(1)}_{m,n} = \phi^{(3)}_{m,n} = (1 - \alpha)\varepsilon_{m,n}, \tag{C1b}$$

$$\phi^{(2)}_{m,n} = \phi^{(4)}_{m,n} = \alpha\varepsilon_{m,n}, \tag{C1c}$$

where we have defined the dimensionless quantity $\varepsilon_{m,n} \equiv [E - V(\boldsymbol{r}_{m,n})] l/\hbar v$. The parameter α can be chosen arbitrarily. We wish to show that the choice $\alpha = 0$ is optimal. We substitute Eq. (3.2a) into Eq.(3.2b) of Sec. III, with this parametrization, and obtain

$$Z^{(1)}_{m,n} = \frac{e^{i\varepsilon_{m,n}}}{2}\{e^{-i\alpha(\varepsilon_{m,n+1} - \varepsilon_{m,n})}[Z^{(1)}_{m,n+1} + Z^{(3)}_{m+1,n+1}] + Z^{(1)}_{m-1,n} - Z^{(3)}_{m,n}\}, \tag{C2a}$$

$$Z^{(3)}_{m,n} = \frac{e^{i\varepsilon_{m,n}}}{2}\{Z^{(1)}_{m,n} + Z^{(3)}_{m+1,n} - e^{-i\alpha(\varepsilon_{m,n-1} - \varepsilon_{m,n})} \times [Z^{(1)}_{m-1,n-1} - Z^{(3)}_{m,n-1}]\}. \tag{C2b}$$

Now we expand in $\varepsilon_{m,n}$, keeping terms to first order, and take $Z^{(1)}$ and $Z^{(3)}$ to be functions defined for all $\boldsymbol{r}$ and smooth on the scale of the lattice. From Eq. (C2) we then obtain

$$0 = [E + \sigma_z p_x + \sigma_x p_y - V(\boldsymbol{r})]\begin{pmatrix} Z^{(1)} \\ Z^{(3)} \end{pmatrix} - \frac{\alpha}{2}\begin{pmatrix} V(\boldsymbol{r} + \boldsymbol{a}_2) - V(\boldsymbol{r}) & V(\boldsymbol{r} + \boldsymbol{a}_2) - V(\boldsymbol{r}) \\ V(\boldsymbol{r}) - V(\boldsymbol{r} - \boldsymbol{a}_2) & V(\boldsymbol{r} - \boldsymbol{a}_2) - V(\boldsymbol{r}) \end{pmatrix}\begin{pmatrix} Z^{(1)} \\ Z^{(3)} \end{pmatrix}. \tag{C3}$$

After transforming to $\Psi = \mathcal{G}(Z^{(1)}, Z^{(3)})^T$, with $\mathcal{G}$ as in Eq. (3.5), the first term on the RHS. of Eq. (C3) becomes the desired Dirac equation. If we choose $\alpha \neq 0$ then the potential V has to be smooth on the scale of the lattice, for the second term to be negligible in comparison with the first. We conclude that $\alpha = 0$ is the optimal choice.

[1] A. H. Castro Neto, F. Guinea, N. M. R. Peres, K. S. Novoselov, and A. K. Geim, arXiv:0709.1163, Rev. Mod. Phys. (to be published).
[2] J. W. McClure, Phys. Rev. **104**, 666 (1956).
[3] M. P. A. Fisher and E. Fradkin, Nucl. Phys. B **251**, 457 (1985).
[4] A. W. W. Ludwig, M. P. A. Fisher, R. Shankar, and G. Grinstein, Phys. Rev. B **50**, 7526 (1994).
[5] D.-H. Lee, Phys. Rev. B **50**, 10788 (1994).
[6] K. Ziegler, Europhys. Lett. **31**, 549 (1995).
[7] J. T. Chalker and P. D. Coddington, J. Phys. C **21**, 2665 (1988).
[8] C.-M. Ho and J. T. Chalker, Phys. Rev. B **54**, 8708 (1996).
[9] B. Kramer, T. Ohtsuki, and S. Kettemann, Phys. Rep. **417**, 211 (2005).
[10] A. K. Geim and K. S. Novoselov, Nat. Mater. **6**, 183 (2007).
[11] K. Hirose, T. Ohtsuki, and K. Slevin, Physica E (Amsterdam) **40**, 1677 (2008).
[12] J. Tworzydło, B. Trauzettel, M. Titov, A. Rycerz, and C. W. J. Beenakker, Phys. Rev. Lett. **96**, 246802 (2006).
[13] H. Schomerus, Phys. Rev. B **76**, 045433 (2007).
[14] Ya. M. Blanter and I. Martin, Phys. Rev. B **76**, 155433 (2007).
[15] A. Rycerz, J. Tworzydło, and C. W. J. Beenakker, Europhys. Lett. **79**, 57003 (2007).
[16] J. H. Bardarson, J. Tworzydło, P. W. Brouwer, and C. W. J. Beenakker, Phys. Rev. Lett. **99**, 106801 (2007).
[17] K. Nomura, M. Koshino, and S. Ryu, Phys. Rev. Lett. **99**, 146806 (2007).
[18] P. San-Jose, E. Prada, and D. S. Golubev, Phys. Rev. B **76**, 195445 (2007).
[19] Infinite-mass boundary conditions are obtained by sending the mass to infinity for $y < 0$ and $y > W$. Particles are thus excluded from this region, much as an infinite potential excludes Schrödinger particles. As a result the boundary condition of Eq. (2.4) is imposed at the boundaries $y = 0$ and $y = W$ between the finite- (or zero) mass and the infinite-mass regions. For more details, see Ref. 21.
[20] J. Martin, N. Akerman, G. Ulbricht, T. Lohmann, K. von Klitzing, and A. Yacoby, Nat. Phys. **4**, 144 (2008).
[21] M. V. Berry and R. J. Mondragon, Proc. R. Soc. London, Ser. A **412**, 53 (1987).
[22] J. L. Pichard and G. Sarma, J. Phys. C **14**, L127 (1981).
[23] A. MacKinnon and B. Kramer, Z. Phys. B: Condens. Matter **53**, 1 (1983).
[24] H. Tamura and T. Ando, Phys. Rev. B **44**, 1792 (1991).